CCFE
CULHAM CENTRE FOR FUSION ENERGY

UK Atomic Energy Authority

UKAEA-CCFE-PR(23)161

J. Hargreaves, H. Tipping, J.C. Eloi, L. Harding, H. Dominguez Andrade, H. Dawson, T.L Martin

The Transient Thermal Ageing of Eurofer 97 by Mitigated Plasma Disruptions in DEMO

The Transient Thermal Ageing of Eurofer 97 by Mitigated Plasma Disruptions in DEMO

J. Hargreaves, H. Tipping, J.C. Eloi, L. Harding, H. Dominguez Andrade, H. Dawson, T.L Martin

This is a preprint of a paper submitted for publication in Acta Materialia

The Transient Thermal Ageing of Eurofer 97 by Mitigated Plasma Disruptions in DEMO

J. Hargreaves[a], H. Tipping[a*], J.C. Eloi[b], L. Harding[a], H. Dominguez Andrade[a], H. Dawson[c], and T.L Martin[a]

[a] *University of Bristol, H.H. Wills Physics Laboratory, Tyndall Avenue, Bristol, BS8 1TL, UK*
[b] *University of Bristol, School of Chemistry, Tyndall Avenue, Bristol, BS8 1TL, UK*
[c] *UKAEA, Culham Centre for Fusion Energy, Culham Science Centre, Abingdon, Oxfordshire, OX14 3DB*
**corresponding author: hannah.tipping@bristol.ac.uk*

Abstract

Severe plasma transients such as disruptions will impose high magnitude, short duration thermal loads on the plasma-facing first wall of the EU's DEMOnstration tokamak. Repeated over DEMO's lifetime, these transients may cumulatively alter the microstructure of first wall structural materials, degrading their performance. The effects of repeated mitigated disruptions on the microstructure of the reduced activation ferritic/martensitic steel Eurofer 97 is reported. Time-dependent finite element thermal analysis of mitigated disruption heating on DEMO's water-cooled lithium lead (WCLL) blanket concept has been used to design a novel laser-based transient thermal exposure experiment. The microstructural evolution of Eurofer 97 under these dynamic thermal loads has been studied via a variety of scanning and transmission electron microscopy techniques, and micromechanical testing. Just one 700°C thermal transient was found to promote grain coarsening and partial recrystallisation. Further exposure resulted in significant grain growth and a reduction of grain aspect ratios. The nucleation and coarsening of $Cr_{23}C_6$ at grain boundaries and V-rich and Ta-rich MX precipitates within the ferritic matrix was also observed. The microstructural evolution resulting from 850°C transients is also reported. After 1000 transients at 850°C, Eurofer 97's hardness was decreased by 32%.

Keywords: Fusion, Eurofer 97, disruptions, plasma-material interaction, thermal ageing

1. Introduction

In a tokamak fusion reactor, highly energetic plasmas are generated and confined using strong magnetic fields. These electrically conductive and magnetic fusion plasmas are prone to turbulent magnetohydrodynamic instabilities which can challenge the magnetic confinement of the plasma, causing it to deposit a thermal load on the plasma facing first wall.

Plasma transients such as major disruptions and edge localised modes (ELMs) pose an acute hazard to the plasma-facing components of a tokamak [1]. These highly energetic plasma-wall interactions (PWI) can impose short-duration, high-magnitude thermal and charged particle loads on the plasma-facing first wall (FW), and have been observed to cause melting, erosion, and cracking of plasma-facing surfaces in existing experimental-scale tokamaks [2]–[4].

Plasma disruptions are considered especially problematic. During a disruption the stable magnetic confinement of the plasma is suddenly terminated, and 50-100% of the plasma's thermal and current energy is rapidly quenched by plasma-facing surfaces [5]. Disruptions are a frequent occurrence in existing tokamaks – for example, approximately 6% of H-mode plasma discharges in the Joint European Torus (JET) between 2000-2007 were terminated by an unanticipated disruption [6]. Advancements in magnet systems may make disruptions less frequent in newer tokamak designs, however the ITER experimental fusion reactor (presently under construction) is expected to experience as many as 2,600 disruptions in its 30-year lifetime [11]. In a commercial-scale reactor prototype with a much larger

plasma volume such as the DEMOnstration fusion power station (DEMO), even a single disruption is considered to pose an intolerable risk of severe thermal damage to plasma-facing components [7], [8].

To manage these risks, the DEMO tokamak will be protected by active disruption mitigation measures such as shattered pellet injection (SPI) or massive gas injection (MGI) [9], [10]. Many FW concept designs for DEMO also employ sacrificial limiters and a protective layer of tungsten. Despite these measures, mitigated disruptions are presently estimated to impose 1-2 GW m^{-2} on DEMO's FW for a duration of 1-3 ms [9]. This transient load is likely to briefly subject the structural material underlying DEMO's FW to temperatures beyond its design maximum [12].

The leading structural material candidate for DEMO's FW is Eurofer 97, a reduced activation 9Cr ferritic/martensitic steel specifically developed for fusion reactor structural applications. Eurofer 97's novel reduced activation composition (8.95Cr, 0.11C, 0.55Mn, 0.022N_2, 0.12Ta, 0.202V, 1.06W, balance Fe. (w.t.\%)) may give rise to unexpected behaviour in the challenging fusion environment, thus the effects of both isothermal and repeated transient thermal exposure on its microstructure and mechanical properties must be comprehensively understood prior to its use.

Prior work on the isothermal ageing of Eurofer 97 found that short-term (168 h) isothermal annealing at 550-650°C had a negligible effect on Eurofer 97's microstructure [12], but 5,000 hours exposure to 500-550°C causes the progressive breakdown and partial recrystallisation of Eurofer 97's tempered martensite sub-grains, and the coarsening of its existing Cr-rich $M_{23}C_6$ and MX-type precipitates [13], [14]. Isothermal annealing for 168 hours at higher temperatures of 700-850°C produced similar microstructural effects and was also accompanied by the nucleation and growth of new Cr-rich secondary phase precipitates (likely $Cr_{23}C_6$) at prior-austenite grain (PAG) boundaries [12].

Short-term, high temperature isothermal annealing (800°C for 5 minutes) after cold rolling was found to have a profound microstructural effect. Eurofer 97's fine tempered martensitic sub-grains were replaced by a heterogenous microstructure consisting of pockets of partially recrystalised sub-grains, which were surrounded by large coarsened equiaxed grains. Abnormal grain growth and precipitate coarsening was also observed [15]. After 4 hours of isothermal exposure at 850°C similar effects were seen, accompanied by the formation of small pockets of virgin martensite suggesting some degree of austenitisation. 24 hours of isothermal annealing at 850°C (followed by quenching) found that a significant majority of Eurofer 97's coarsened grains were replaced by new virgin martensite [12].

While much data exists on Eurofer 97's isothermal ageing behaviour, relatively few studies have explored the effects of transient thermal exposure [12]. Repeated over the lifetime of the DEMO reactor, thermal transients imposed by mitigated disruptions may pose a novel transient thermal degradation mechanism with serious potential to significantly alter Eurofer 97's material properties. Consequently, the performance of DEMO's FW may be degraded over time. This paper seeks to explore the transient thermal degradation of Eurofer 97 via a laser-based transient exposure experiment, supported by thermal analysis simulations of estimated disruption thermal loads on a leading concept design for DEMO's FW.

2. Method

2.1 Finite Element Thermal Analysis

Time-dependent thermal analyses were conducted using Comsol Multiphysics 5.4 to estimate the temperature rise experienced by Eurofer 97 in DEMO's FW during a mitigated disruption. An outboard module of DEMO's 2019 single module segment (SMS) water-cooled lithium-lead (WCLL) FW concept was used for all analyses [16], [17]. Preliminary thermal analysis reported previously ([12]) determined that the WCLL's side walls, baffles and lithium-lead breeding material would be unaffected

during a mitigated disruption, thus the region of interest (ROI) for this study was restricted to the WCLL's front wall and adjacent 90° elbows. A 3D model of this ROI was de-featured, partitioned, and meshed into 10^5 tetrahedral elements with a mean skewness of 0.40.

Temperature-dependent thermophysical property expressions for Eurofer 97 were employed where available, and values for ASTM P91 or P92 steel (Eurofer 97's non-reduced activation 9Cr steel analogues) were substituted where necessary [18], [19]. Two separate fluid domains were configured for coolant flow, for alternating counter-current and co-current coolant channels respectively. Initial temperatures were applied to the model based on published steady-state WCLL thermal analyses [16], [17]. Key parameters are summarised by Table 1.

Table 1. Summary of key thermal FEA parameters.

Parameter	**Value**	**Units**	**Reference**
Eurofer 97 front wall initial temperature	397	°C	[17]
Tungsten armour initial temperature	422	°C	[17]
Tungsten emissivity	0.39	-	[20]
PbLi temperature (constant)	408	°C	[11]
Mean Coolant temperature	310	°C	[11]
Coolant velocity	2.0	m s^{-1}	[11]
Coolant pressure	15.5	MPa	[12]
Mit. disruption thermal load	2000	W m^{-2}	[8], [9]
Mit. Disruption duration	3	ms	[8], [9]

Boundary conditions were applied based on the following assumptions: (i) The wetted area of a disruption is sufficiently large that the applied thermal load will be uniform, and vertical symmetry can be assumed [21]. (ii) In addition to conductive and convective cooling, the affected plasma-facing area cools radiatively after a disruption to unaffected plasma-facing surfaces at 422°C [17]. To simulate a mitigated disruption, at the start of each study a heat flux load of 2000 MW m^{-2} was applied to plasma facing surfaces for 3.0 ms [9]. Results are presented in section 3.1.

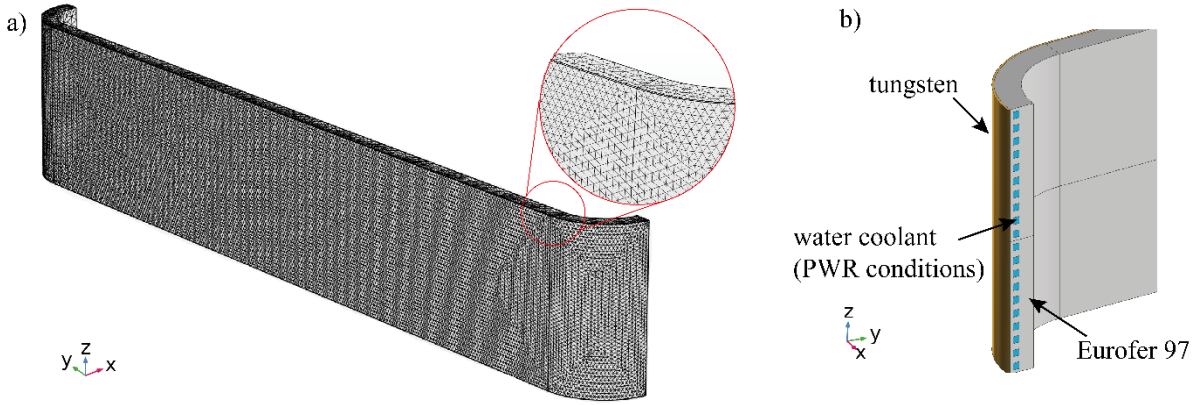

Figure 1. Region of interest after meshing (a) and detail of elbow (b), annotated with material domains.

2.2 Sample Preparation and Laser Transient Thermal Exposure

Thermal FEA results were used to determine target temperatures and heating/cooling rates for a transient thermal exposure experiment. To prepare samples for this, a 6 mm rolled plate of Eurofer-97 was sectioned into 8×8×0.5 mm samples using a water-cooled Struers Accutom 50 diamond disc sectioning saw. The saw feed rate was restricted to a max. of 0.05 mm min^{-1} to prevent cutting damage.

Prior to transient exposure a tungsten-based plasmonic surface was fabricated on the laser-incident face of each sample to improve its absorptivity of 10.6 µm wavelength light. Details of this plasmonic grating are given in [22]. The application of this functional surface was verified via electron microscopy to have a negligible effect on the bulk microstructure of the Eurofer 97 samples.

The transient exposure apparatus consists of a continuous wave 40 W CO_2 laser (Synrad Inc. Firestar V40 series), directed through three gold mirrors and a ZnSe window into a vacuum vessel [23]. The emitted infra-red beam has a wavelength (λ) of 10.6 µm and a gaussian intensity profile with a quality factor of 1.2. Its beam waist diameter at the outlet aperture is 2.5 mm, with a full angle divergence of <7 mrad [24]. The beam waist diameter at the sample stage is estimated to be 6 mm, incident at an angle of 90°.

The combined optical losses of the laser apparatus have been measured at 9 - 27%, thus the maximum beam power incident on the sample is estimated to be 29.2 - 36.4 W. Sample temperature is continuously measured by temperature transmitter TT1, a non-contact dual-detector spot pyrometer (λ_1 = 1.0, λ_2 =1.5 µm) with a resolution of 0.1°C and a maximum uncertainty of 2.0°C. TT1 is directed at the laser-incident sample face through another borosilicate glass window, and a gold mirror. A local PC running LabView 2019 is employed for data acquisition and automated laser control.

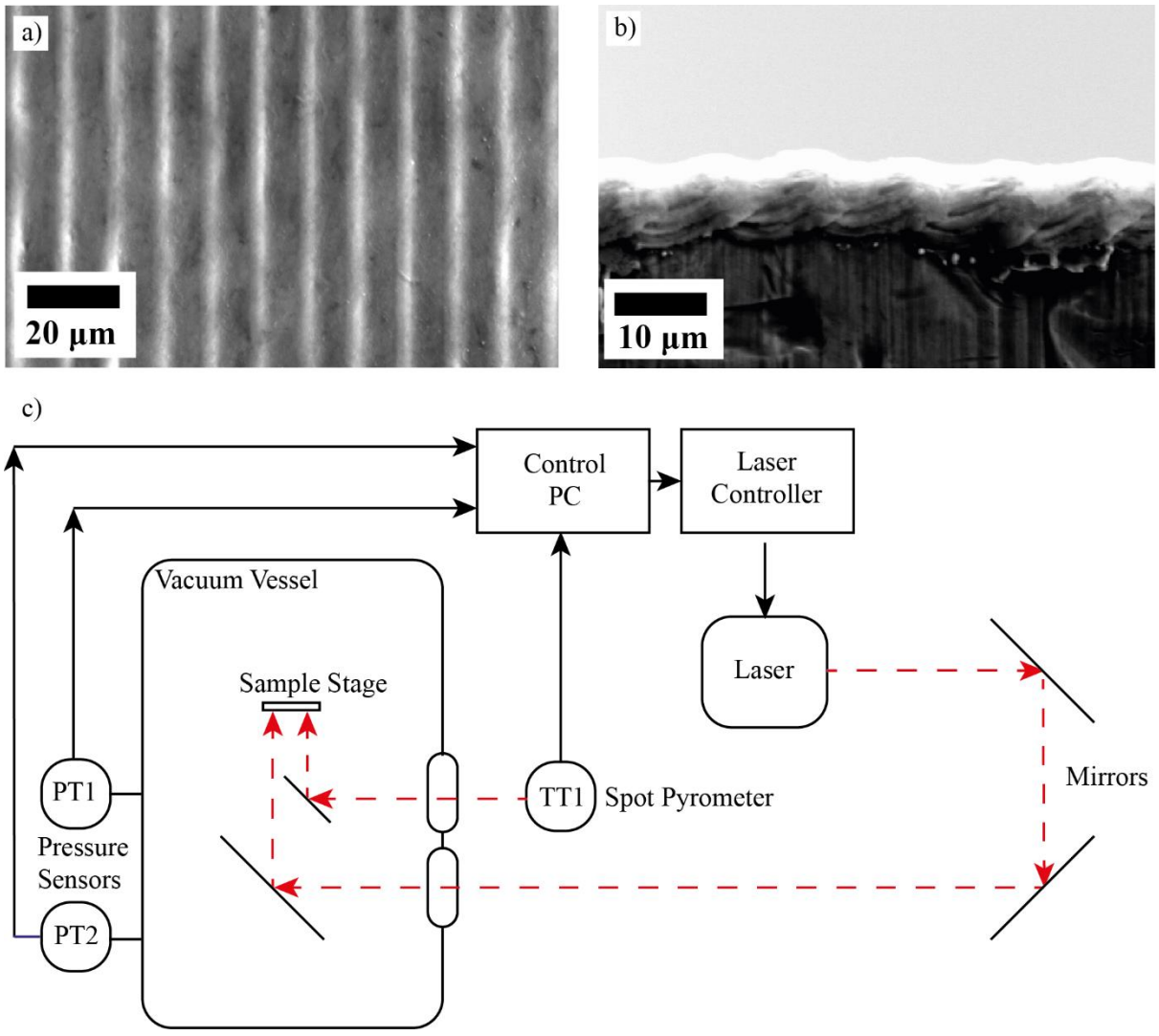

Figure 2. Preparation of the laser incident face prior to W-deposition (a) top view, (b) side view, and (c) schematic diagram of the laser-based transient thermal exposure apparatus.

2.3 Microstructural and Micromechanical Characterisation

The microstructural effects of transient thermal exposure were studied via various scanning and transmission electron microscopy techniques, as well as micromechanical hardness testing. To prepare samples for electron microscopy, as-received and thermally-exposed samples of Eurofer 97 were mounted in conductive thermosetting resin, and the non-laser incident face of each sample was ground to a 5 μm finish using progressively finer SiC papers. These were sequentially polished with 3 μm, 1 μm and 0.25 μm diamond pastes for 10 minutes each, then vibro-polished for 24 hours in a suspension of 50 nm colloidal silica. Finally, samples were ultrasonically cleaned using acetone, ethanol and isopropanol. Further details on the sample preparation procedure are given by [25].

Scanning electron microscopy employed a variable-pressure (VP) Zeiss SigmaHD field emission gun scanning electron microscope (FEGSEM) equipped with secondary electron (SE) and angle-selective backscattered electron (AsB) detectors. Images were collected at an accelerating voltage of 10-20 kV, aperture of 30 μm, and working distances of 4-10 mm. The ORS Dragonfly and ImageJ software packages were employed for thresholding and precipitate statistics.

SEM elemental analysis using an EDAX Octane Elect energy-dispersive X-ray (EDX) spectrometer was performed in VP mode at 20 kV, an aperture of 120 μm, and an amp time of 0.24 μs. Electron Backscatter Diffraction (EBSD) was conducted at a specimen tilt of 70°, beam voltages of 25-30 kV, and an aperture of 120 μm using either an Oxford Instruments Symmetry S3 detector or an EDAX Velocity Pro detector EBSD data was conservatively processed using the AztecCrystal or OIM Analysis softwares. Wild spikes and zero solutions (8 neighbours) were removed, and a quadrant-type Kuwahara filter with a radius of 3 was applied. Kernel average misorientation maps were generated using 5x5 pixel binning and a bin width of 0.1.

Transmission electron microscopy (TEM) foils with approximate dimensions 30×20×0.1 μm were extracted in-situ from the centre of selected laser-exposed samples using a FEI Helios 600i Nanolab Dualbeam focused ion beam (FIB) and electron microscope, equipped with a Kleindiek micromanipulator and a Pt deposition needle. Trenching was conducted at beam currents of 6.5 – 21 nA, and fine polishing at 0.17 nA – 0.92 nA. Prior to trenching a 30×4×4 μm Pt strip was deposited on top of the extraction site as per [26]. The extracted foils were analysed via bright field imaging and selective area electron diffraction (SAED) using a 200 kV JEOL 2100 field emission transmission electron microscope. TEM-EDS mapping was conducted using an Oxford Instruments X-Max 80T detector at an amp time of 0.24. Hardness testing of all samples was conducted in accordance with ISO 6507-1 using a Buhler Micromet 6030 indenter with a Vickers diamond tip. The applied load was ~4900 mN and the dwell time was 10 seconds, with a load/unload time of 3 seconds.

3. Results

The results of the thermal FEA analysis are presented first, with predictions of the maximum Eurofer 97 temperatures reached during a mitigated disruption, and the time taken for Eurofer 97 in the WCLL to cool to normal operating temperature. This is followed by an analysis of temperature data from the laser transient thermal exposure experiment. Finally, the results of microstructural characterisation of transient-exposed Eurofer 97 are presented, along with micro-hardness test data.

3.1 Thermal Analyses of Mitigated Disruption heating on the WCLL

To monitor temperatures during and after the simulated disruption, virtual thermocouples were inserted in the centre of the front wall at the tungsten surface and throughout the Eurofer 97 in 0.2 mm increments from the tungsten-Eurofer 97 interface. The Eurofer 97 temperatures estimated are reported in Fig. 3.

The model predicts that a mitigated disruption (2000 MW m^{-2} for 3 ms) will quickly increase the surface temperature of the WCLL's tungsten armour to a maximum of 1208°C. The maximum temperature Eurofer 97 reached was 956 °C, occurring 72 ms after the end of the disruption due to thermal resistivity effects. This temperature increase was initially localised to the Eurofer 97 region adjacent to its tungsten interface, however 1.2 seconds after the end of the disruption its thermal energy had conducted throughout the first wall to reach the coolant channels.

The cooling arrangements of the WCLL front wall are highly effective, and within 2.4 seconds of the disruption ending all regions of the Eurofer 97 domain were predicted to cool below its maximum design temperature of 550°C [5]. However, the water coolant is predicted to experience a significant temperature increase, and local vaporisation of the coolant within the front wall cooling channels is predicted to occur.

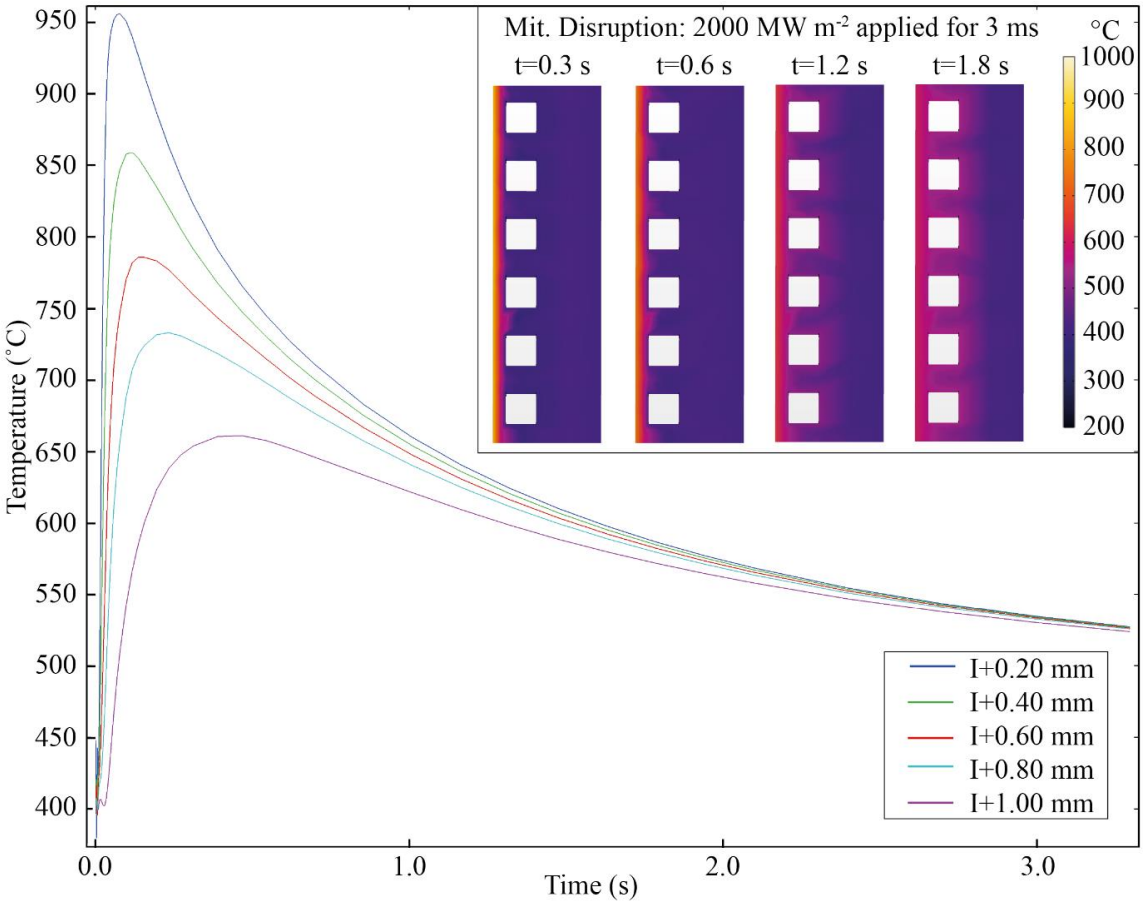

Figure 3. Temperature profile of front wall Eurofer 97 during a mitigated DEMO disruption, tungsten omitted. 'I' represents the Eurofer 97-W interface. Inset: Cross-sections through the Eurofer 97 domain.

3.2 Transient Thermal Exposure

Two series of Eurofer 97 samples were exposed to thermal transients with peak temperatures of 700°C and 850 °C respectively. Exposure at these temperatures was repeated 1, 10, 100, 500 and 1,000 times

on separate samples. One sample was also exposed to 850°C transients 1,500 times. Between each transient, samples passively cooled to 400°C, the mean temperature of Eurofer 97 at the WCLL front wall during normal operation [1][2]. The passive cooling mechanisms were heat radiation to the chamber walls and heat conduction from the sample to the sample holder stage. There was no convective cooling, as to prevent sample oxidation the pressure in the vacuum vessel was kept at approximately 7.5×10^{-5} m Torr throughout each exposure run.

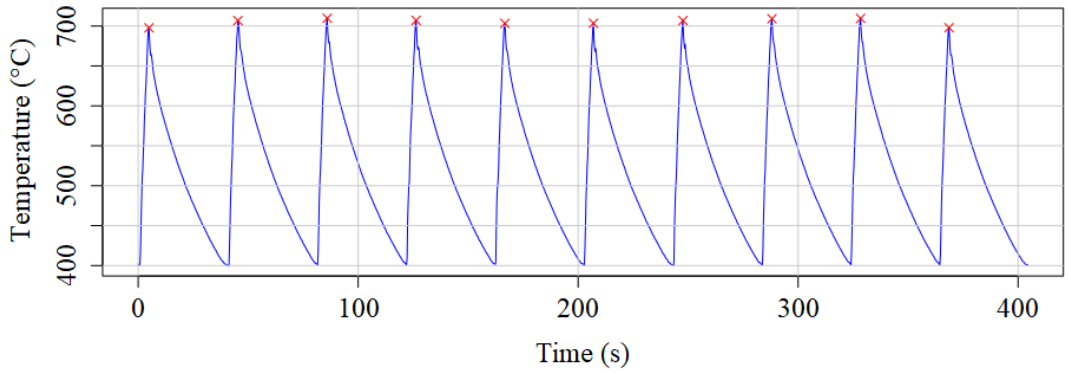

Figure 4. Temperature data showing a subset of 10 transients at 700°C, measured by spot pyrometer TT1.

The mean heating rates achieved across the 700 and 850°C series were 52 °C s^{-1} and 39 °C s^{-1} respectively, and the mean cooling rates were 6.7 °C s^{-1} and 5.8 °C s^{-1} respectively. The laser heating method was accurate and highly repeatable - standard deviation (SD) from the target temperatures ranged from 2.5 - 7.0°C across the 700°C and 850°C series. An outlier was the 1500 transient sample, which had a SD of 12.1°C from its 850°C target temperature. This was likely due to partial degradation of the nanophotonic surface after ~1,000 transients, which was compensated for by manually increasing the duration of the laser pulse. The total heating time of the 1,500 transient sample was 41 hours.

3.3 Microstructural Characterisation

3.3.1 As-Received Eurofer 97

As-received Eurofer 97 exhibits a homogenous tempered martensite microstructure with blocks and packets of fine elongated sub-grains 0.1-2 µm in length, located within prior austenite grains 10-11 µm dia. (Fig. 5). Sub-grains aspect ratios are 1:5 to 1:10. Slightly elongated carbides 25-250 nm dia. (likely Cr-rich $M_{23}C_6$) are sparsely located on prior-austenite and sub-grain boundaries, and smaller (10-50 nm dia.) Ta/V-rich spheroidal MX carbides/nitrides. are found within the matrix (Fig. 5b).

EBSD phase analysis detected no retained austenite in the as-received Eurofer 97. $M_{23}C_6$ was omitted from the phase set as it is too crystallographically similar to ferrite for accurate discrimination at this resolution, and so these $M_{23}C_6$ carbides are expected to show up as black (non-indexed) regions on the EBSD images. Sub-grains were too small to be observed on the inverse pole figure (IPF) map (Fig. 5c), however, their boundaries are highlighted by the kernel average misorientation (KAM) map (Fig. 5d).

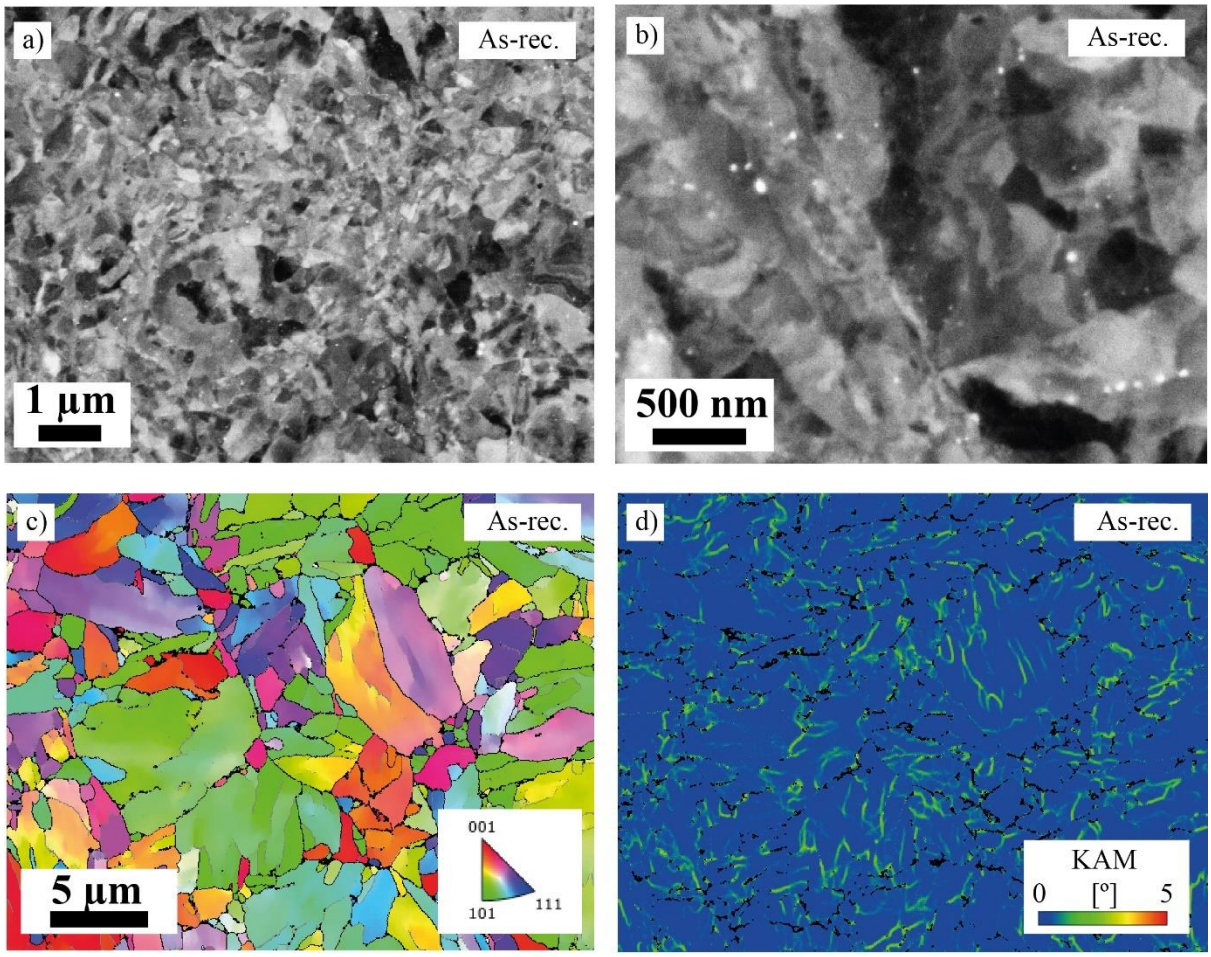

Figure 5. AsB micrographs (a, b), EBSD IPF (c) and KAM maps (d) of as-received Eurofer 97.

3.3.1 The Cumulative Microstructural Effects of 700°C Transients

Exposure to a single 700°C transient (Fig. 6a, b) promoted a significant microstructural evolution. Relative to the as-received condition sub-grain diameters were increased to 0.46 - 2.1 µm dia. and aspect ratios were reduced to 1:4. Some equiaxed grains and partial grain recrystallisation were observed. Precipitate number densities and diameters were negligibly affected after one transient, however after 10 transients a slightly greater number density of precipitates were observed (Fig. 6c).

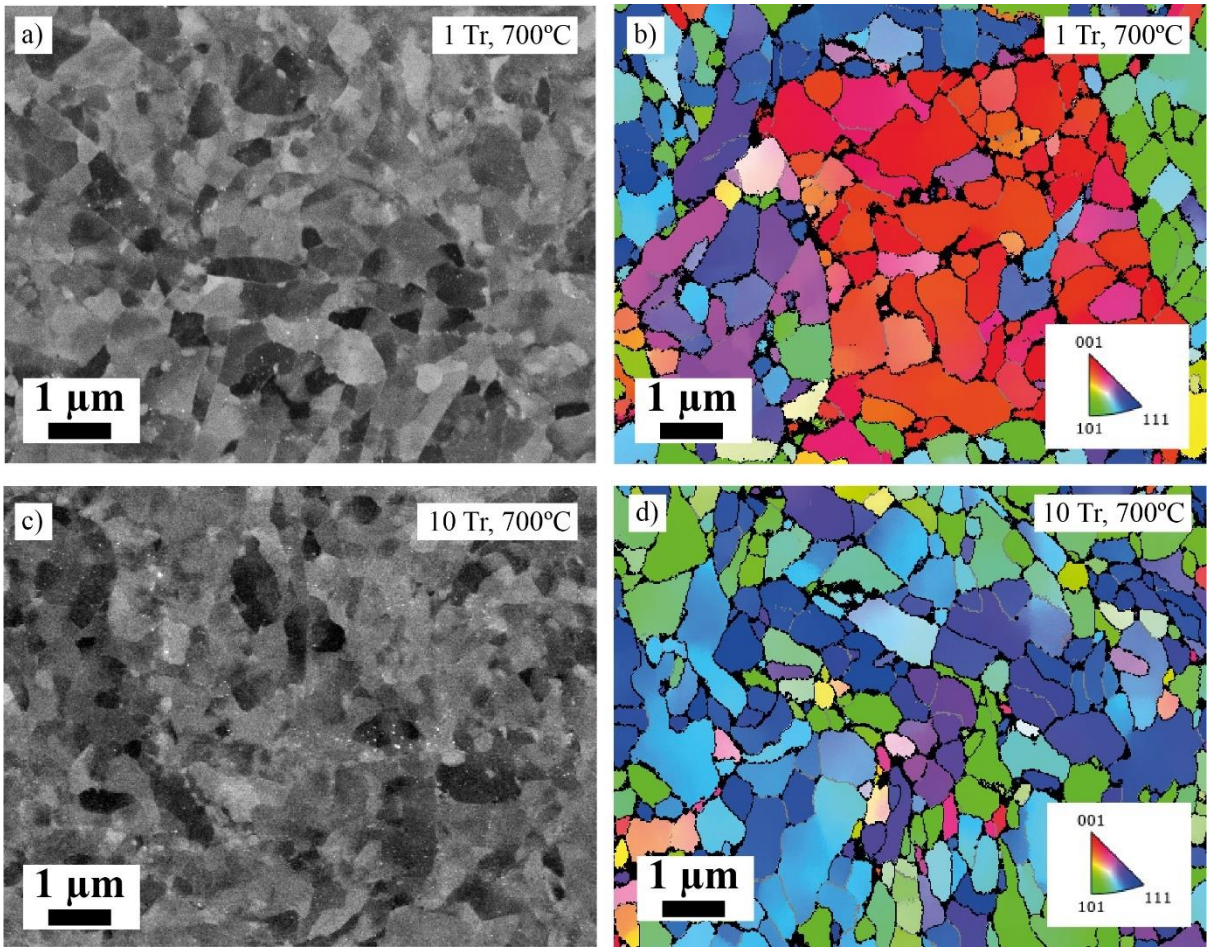

Figure 6. AsB micrographs (a,c) and EBSD inverse pole figure (IPF) maps (b, d) of Eurofer 97 affected by 1 and 10 transients at 700°C.

Exposure to 100 transients at 700°C (Fig 7a) was found to result in the significant nucleation and growth of secondary phases at grain boundaries (GB), accompanied by further coarsening of Eurofer 97's tempered sub-grains (Fig. 7b). Eurofer 97's tempered martensitic packet and block morphology was mostly retained, and coarsened sub-grains appeared in blocks of similar orientation. After 250 transients, sub-grain coarsening was accompanied by a high degree of recrystallisation. Isolated blocks of coarsened sub-grains were surrounded by larger recrystallised grains with similar sizes and aspect ratios as the blocks (Fig. 7d). GB precipitates were observed to elongate and slightly coarsen with further exposure, from 237±89 nm dia. after 100 transients to 283±104 nm after 250 (Fig. 7c, d).

A sharp drop in the number density of precipitates was observed after 500 transients (Fig. 7e, f). This was confirmed by repeating the 500 transient exposure on a fresh sample, after which the same sharp decrease in precipitate number density was observed. After 1000 transients (Fig. 7g, h) a fully recrystallised ferritic microstructure was observed. Grain boundary precipitates had grown to 1008±284 nm dia, and intra-granular precipitates had diameters of 121±32 nm. Corresponding EBSD KAM maps of the transient-affected Eurofer 97 are given in the supplementary data.

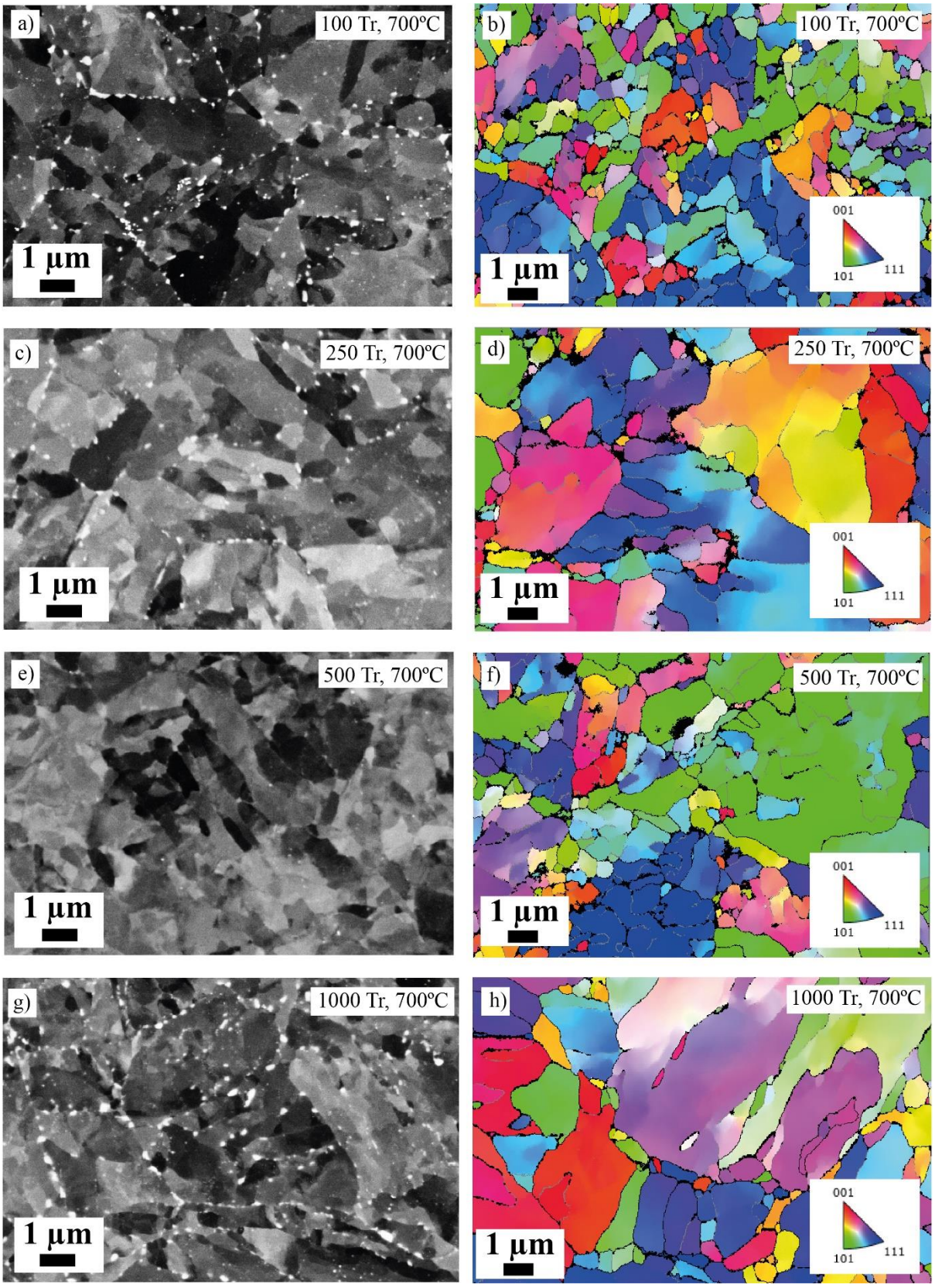

Figure 7. AsB micrographs and EBSD IPF maps of Eurofer 97 after a,b) 100, b,c) 250, d,e) 500 and f,g) 1,000 transients at 700°C. The unindexed regions decorating grain boundaries are likely either $M_{23}C_6$ carbides, or recrystalised ferrite grains that are too small to index.

STEM-EDX mapping of precipitates in Eurofer 97 affected by 100, 250 and 1000 transients at 700°C (Fig. 8) revealed that the larger elongated grain-boundary precipitates are Cr-enriched and co-located with carbon (likely Cr-rich $M_{23}C_6$). Smaller spherical inter-granular precipitates were either Ta-rich and co-located with carbon (likely TaC carbides) or V-rich and mostly co-located with nitrogen (likely VN nitrides). In many cases, TaC carbides and VN nitrides were co-located, often in a conjoined 'V-wing' morphology (Fig. 8a, inset, and Fig. 9 a-d).

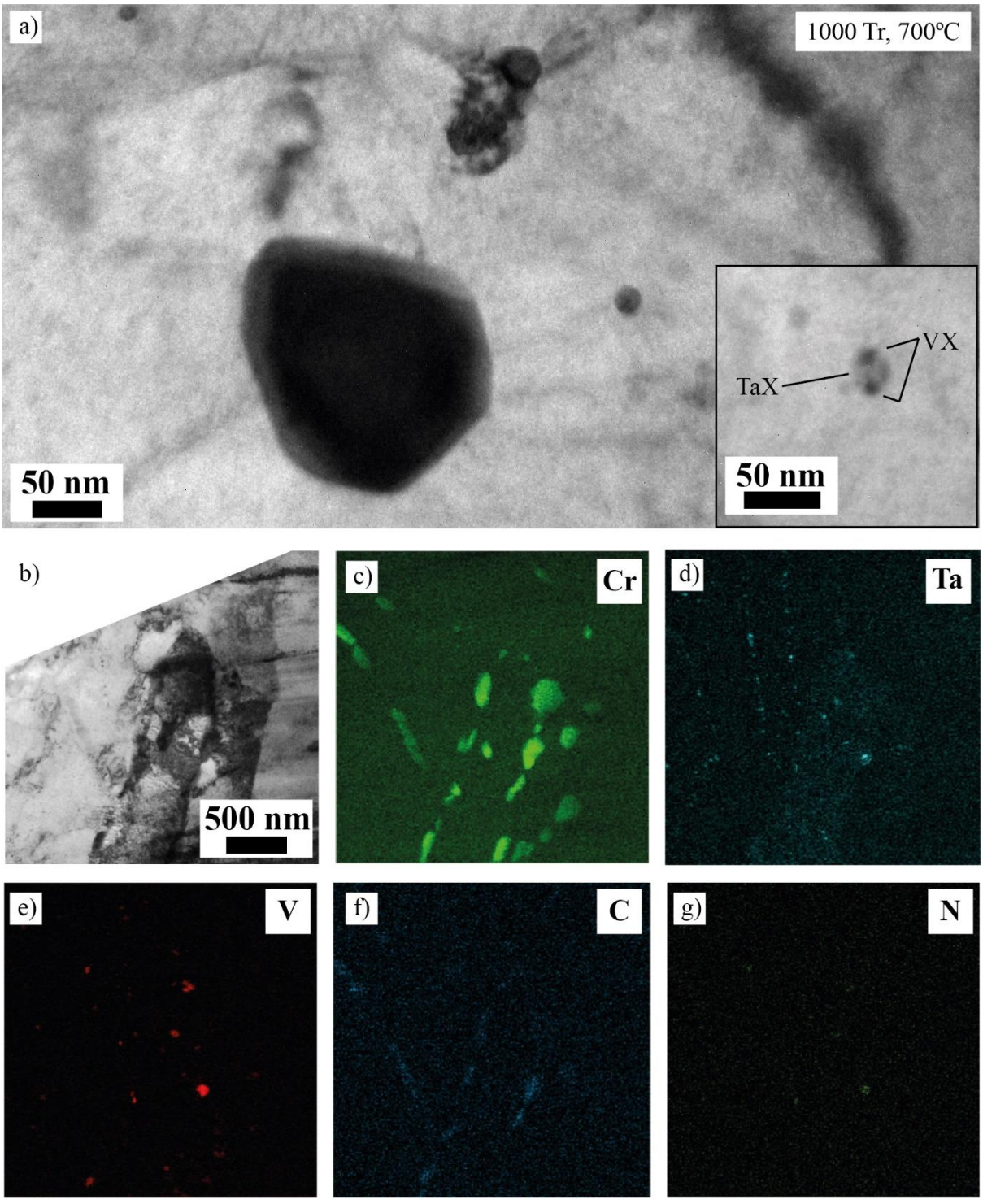

Figure. 8. Examples of precipitates in Eurofer 97 affected by 1,000 transients at 700°C. a) TEM BF images of intra-granular precipitates (inset: a 'V-wing' precipitate). b) TEM BF image of precipitate-decorated grain boundaries c-g) STEM-EDX maps of (b) for Cr, Ta, V, C and N respectively.

Selective area electron diffraction (SAED) patterns of selected Cr-rich and V-rich precipitates in Eurofer 97 affected by 1,000 transients at 850°C are presented in Figs. 9 g & h. Comparison with published SAED patterns from the literature confirmed that the larger Cr-rich and smaller Ta-rich precipitates are $M_{23}C_6$ and MX-type respectively [28], [29].

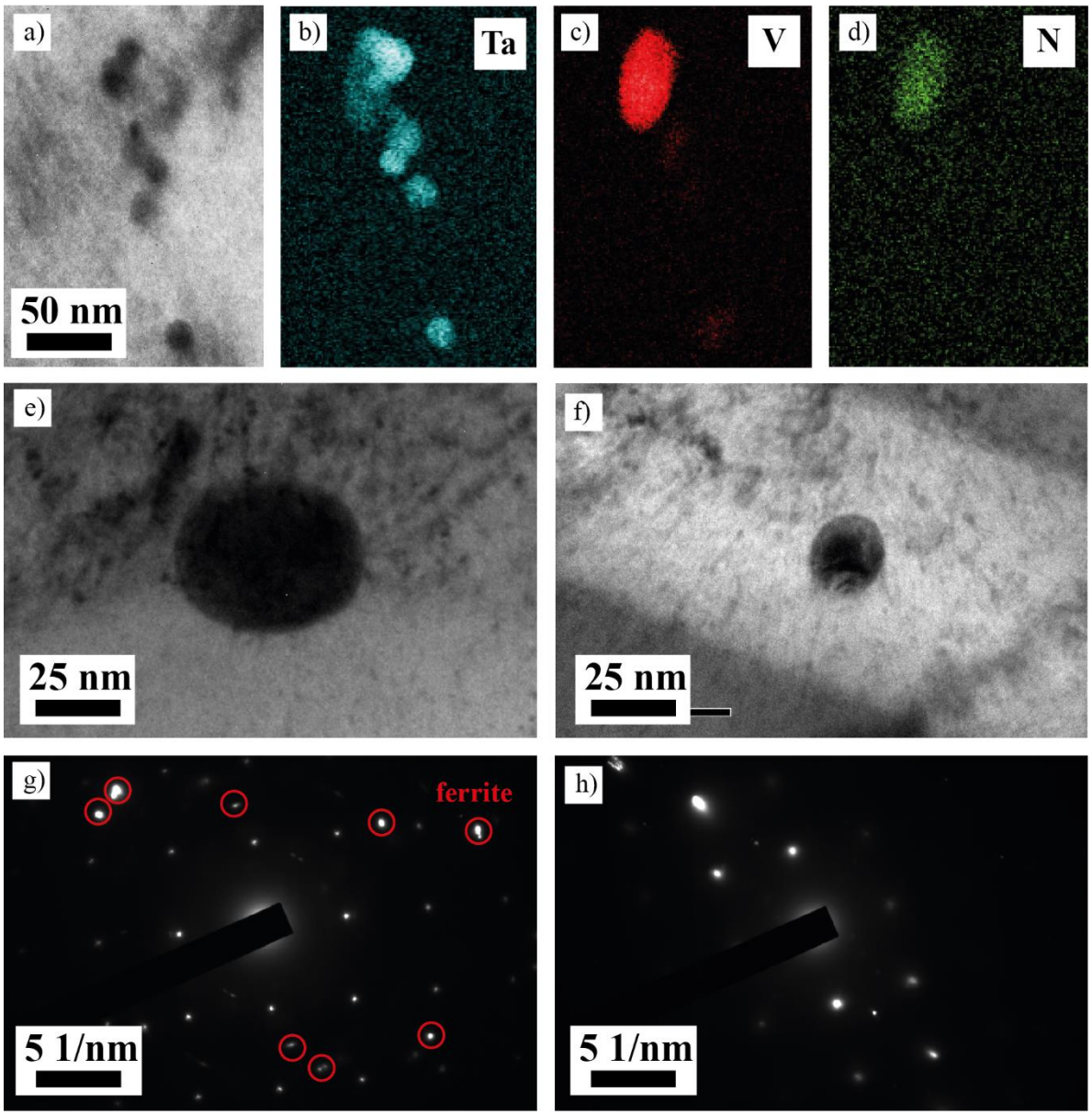

Figure 9. Precipitates in Eurofer 97 affected by 1000 transients at 700°C. a) TEM BF image of a small precipitate cluster, b-d) STEM-EDX maps of (a) for Ta, V, and N respectively. e, f) TEM BF image of a large Cr-rich precipitate and a small Ta-rich precipitate respectively, f, g) SAED patterns of (e, f) respectively.

3.3.1 The Cumulative Microstructural Effects of 850°C Transients

After 100 transients at 850°C (Fig. 10a, b) a significant degree of microstructural evolution had occurred. Coarse ferrite grains 1.1 - 2.3 μm dia. were observed. Most grains were equiaxed, although some elongated grains with aspect ratios of 1:2 to 1:4 were also present. Grain boundaries were sparsely decorated with equiaxed precipitates, which had grown at the expense of smaller ones (Fig 10d).

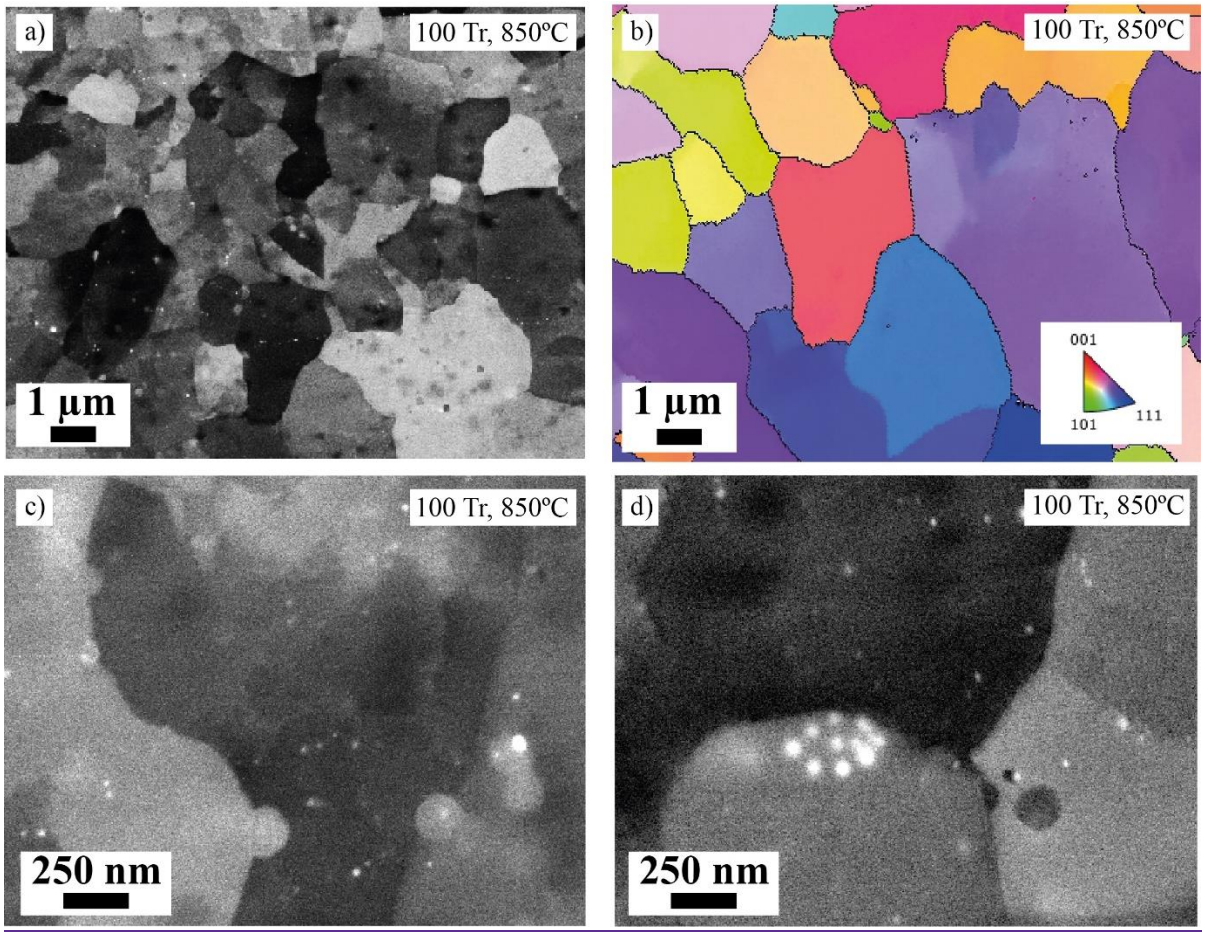

Figure 10. AsB micrographs (a, c, d) and EBSD IFP maps (b) of Eurofer 97 after 100 transients at 850°C.

Further exposure to 250 transients (not shown) did not result in appreciable precipitate nucleation or grain coarsening, suggesting that a degree of metastable thermodynamic equilibrium had been reached.

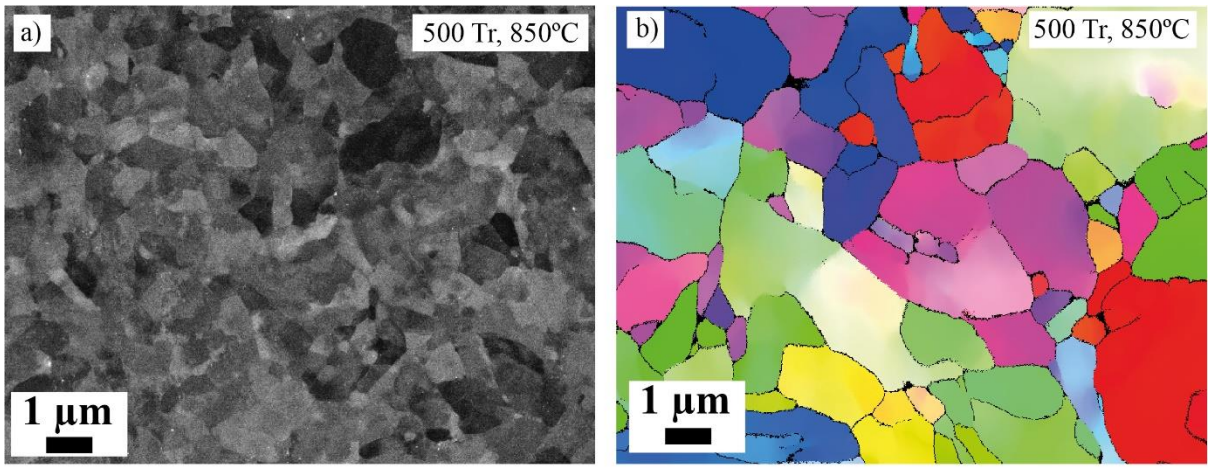

Figure 11. SEM (a) and EBSD (b) maps of Eurofer 97 affected by 500 transients at 850°C.

Exposure to 500 transients (Fig. 11) produced a heterogenous microstructure of fine recrystalised sub-grains surrounded by larger coarsened equiaxed grains. Still relatively few precipitates were observed.

After 1000 transients (Fig. 12), a fully ferrite+carbide microstructure had evolved. Grain sizes changed very little and this was corroborated by EBSD maps (Fig. 12). Large 485±190 nm dia. precipitates were observed to have grown both at grain boundaries and within grains. SEM-EDX determined these to be Cr-rich carbides, also slightly enriched in manganese and tungsten (Fig. 12). Smaller V-rich intragranular precipitates 39±19 nm dia. were also found. Ta-rich precipitates were either notably absent or were too small to be observed.

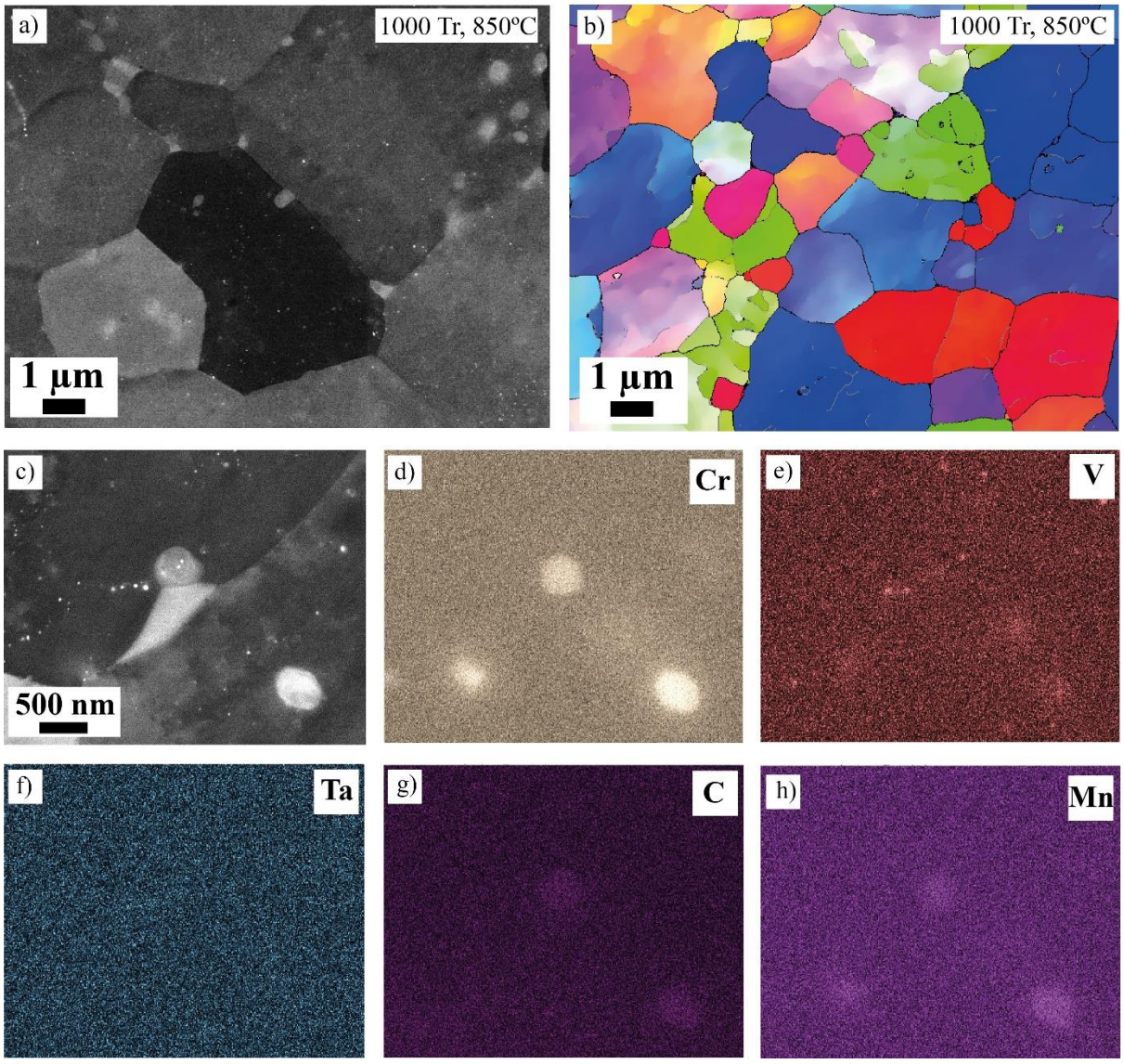

Figure 12. AsB micrograph (a), EBSD IPF map (b) and EDX maps (c-h) of precipitates in Eurofer 97 after 1,000 transients at 850°C.

Prolonged transient exposure (1500 transients) at 850°C caused significant grain growth (Fig. 10). Spot EDX of the 1,500 transient sample found larger precipitates at grain boundaries to be Cr-rich (likely $M_{23}C_6$) and intragranular precipitates to be V-rich and Ta-rich, likely MX-type carbides and nitrides (see supplementary data for spot EDX data).

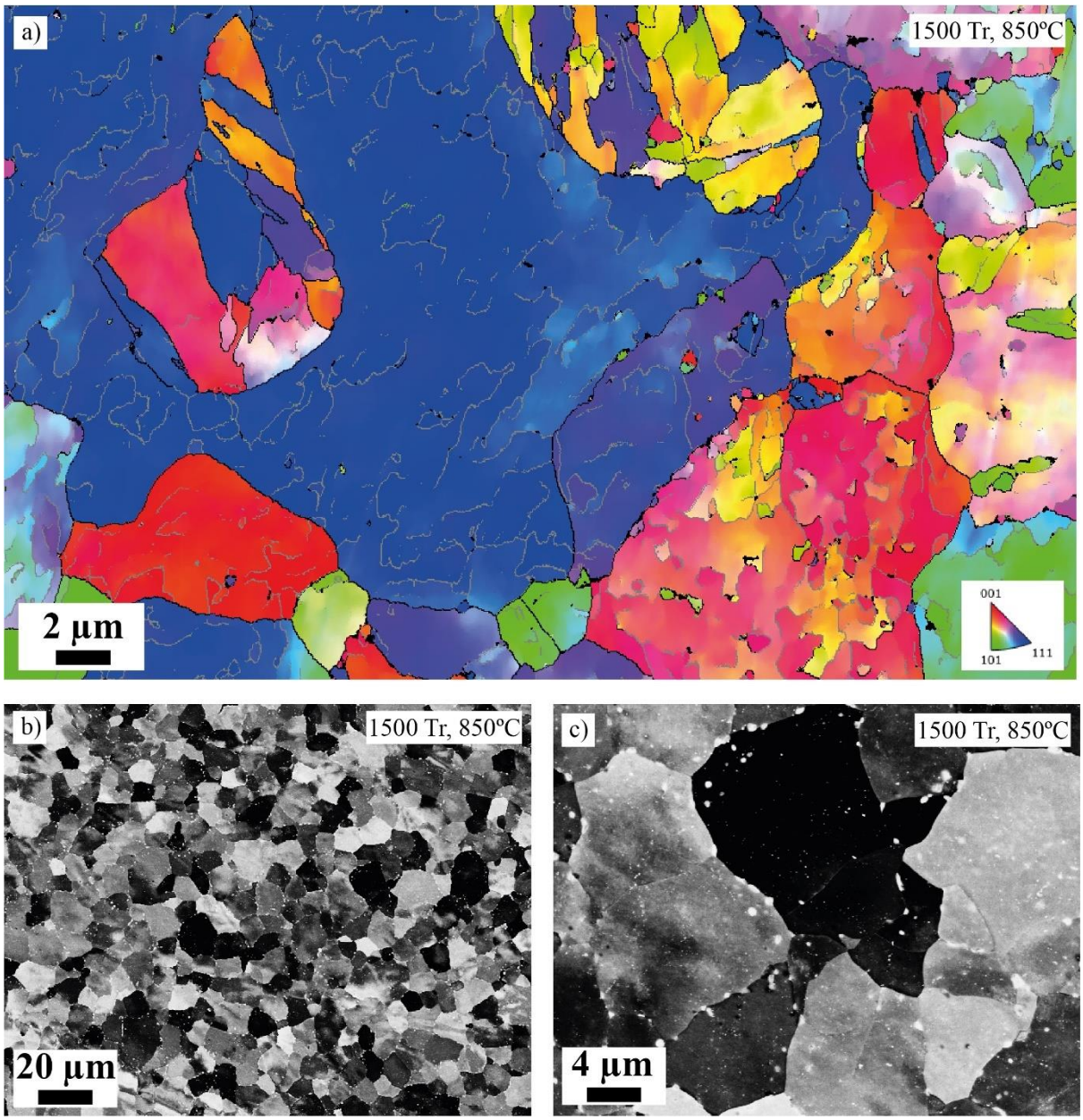

Figure 13. EBSD map (a) and AsB micrographs (b, c) of Eurofer 97 after 1,500 transients at 850°C

3.4 Hardness Testing

Micro-hardness testing data from as-received and transient-affected Eurofer 97 is presented in Fig. 13. Data points represent the mean of 3-6 measurements taken at random from areas near the centre and edges of each sample.

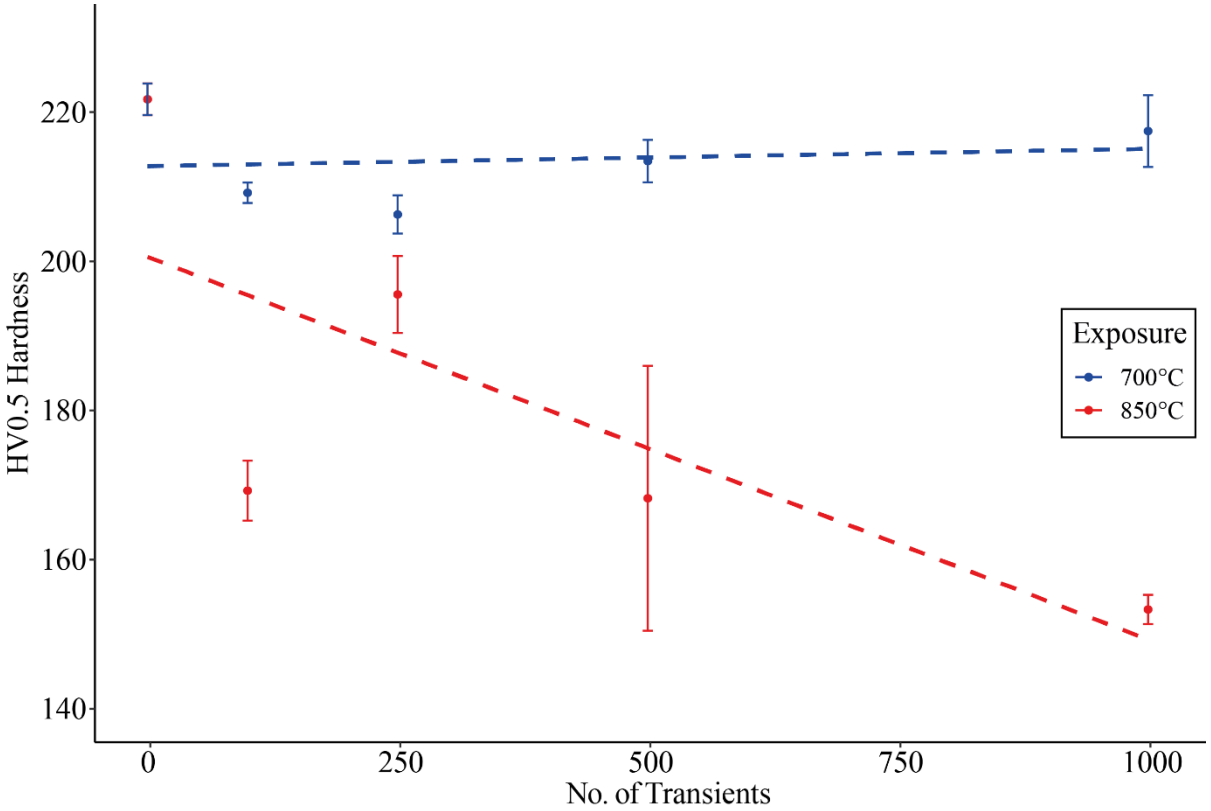

Figure. 14. Hardness data for the 700°C and 850°C series with lines of best fit. Error bars represent standard deviation.

4. Discussion

Thermal FEA modelling predicts that the maximum temperature the WCLL's tungsten armour will experience in the event of a mitigated disruption (2000 MW for 3 ms) is 1208˚C, which is likely below the threshold for tungsten recrystallisation [30]. However, thermal conduction through the tungsten armour briefly heats the underlying Eurofer 97 to a maximum of 956˚C - well beyond its maximum design temperature of 550°C [5]. To determine the cumulative effects on Eurofer 97 of multiple mitigated disruptions over DEMO's operating life, samples of Eurofer 97 were exposed to 700˚C and 850˚C thermal transients using a CO_2 laser. These temperatures were selected as they straddle Eurofer 97's α-γ ferrite transformation temperature of approx. 836°C, and Eurofer 97's phase equilibria in the ferritic and austenitic regimes are distinctively different [12]. At 700°C, Eurofer 97's equilibrium matrix phase is α-ferrite, with stable Cr-rich $M_{23}C_6$, and V and Ta-rich MX-type secondary phases, however at 850°C the matrix phase is γ-austenite and the $M_{23}C_6$ phase fraction decreases until no longer present, while the MX-type phases remain stable [12]. In the lower temperature 700°C series, the presence of Laves phase is also possible, although for the 850°C series it is likely to disappear from the equilibrium matrix and not be observed. Z-phase formation is also possible, however this is unlikely given the extended thermal ageing required (20k+ hours at 650°C [31]) for Z-phase development.

The heating and cooling rates achieved experimentally were within a range of 39-52˚C/s and 5.8-6.7˚C/s respectively. The observed variation of heating/cooling rates is likely due to dimensional inaccuracies during the sectioning stage of sample preparation, and progressive degradation of the plasmonic grating over the course of the experiment which gradually reduces the efficacy of the laser heating. This is demonstrated by the 1500 transient sample at 850°C which exhibited a standard deviation of 12.1°C from its target temperature of 850°C. Comparatively, FEA modelling predicted that during a mitigated DEMO plasma disruption, the temperature of front wall Eurofer 97 would be raised by 550˚C in 75 ms, and cool by 400˚C in 2.4 seconds. The duration of the experimentally achieved transients are thus

approximately an order of magnitude greater than those predicted by thermal analysis, due to the inability of the current apparatus to actively cool the sample. However, the cooling rates achieved by the experiment are still considerably faster than Eurofer 97's critical cooling rate for martensite transformation (0.417 °C s^{-1}) [32].

In contrast to isothermally aged Eurofer 97, which, forms virgin martensite after quenching from 850˚C [12], the laser treated samples exhibit a fully ferritic microstructure with Cr-rich carbides present at the grain boundaries. Although precipitates are observed in the isothermally aged samples, they are considerably larger. After 10,000h at 600°C, significant recrystallisation of sub-grains had occurred in the isothermal samples, and large ~350 nm $M_{23}C_6$ precipitates were observed at grain boundaries [33]. The size difference may be due to the extended thermal exposure experienced, leading to the diffusion of carbon trapped within the martensite. This would be the same cause of precipitate growth for the laser exposed samples however their exposure times is around 200 times shorter leading to smaller precipitate sizes. Due to Eurofer 97s stable equilibrium phases it would be expected that within the 850°C series, the disappearance of the $M_{23}C_6$ precipitates would be observed leaving only TaC and VN phases present. When aged, the precipitate compositions were also altered - the $M_{23}C_6$ phase became enriched in Cr and W, and MX-type carbides became enriched in Ta [14]. In the laser treated samples, the precipitates similarly become enriched in Cr and W, but also experience an enrichment in Mn. Interestingly these Cr-rich precipitates are not present at 500 transients for both the 700˚C and 850˚C samples, possibly due to local hotspots of nitrogen leading to a stabilisation of the austenite phase. The segregation of Cr-rich precipitates to the grain boundaries is an unfavourable effect as it could lead to increased intergranular corrosion [34].

The lower precipitate number density of the 850˚C series, along with its larger grain size, also leads to a decreased hardness. The large standard deviation for the 500 transients is likely due to its heterogeneous microstructure. With fewer precipitates, the material experiences reduced dislocation pinning, allowing the grains to move more freely and reducing the hardness. The larger grain size also means there is less grain boundary present to restrict dislocations. This demonstrates a significant problem as the Eurofer 97 within the front wall must be strong enough to maintain the structural integrity of the reactor. Abnormal grain growth has been reported in isothermally aged samples where coarse grains have reached 10-40 μm [15]. In contrast, the 700°C series experiences a higher hardness possibly due to the presence of Laves phase [12]. Laves lase forms a tight packed crystallographic structure causing notable brittleness and hence an increase in hardness. Although this leads to higher strength, it also makes materials less suitable for structural roles due to their reduced fracture toughness [35].

To improve the method for data collection, a water-cooled stage could be used alongside the laser heating rig to help achieve faster cooling rates, closer to the ones predicted by FEA modelling. To further expand on the results reported in this paper, additional transient heating experiments could be conducted combining techniques such as STEM-EDX, EBSD or atom probe tomography with a scattering experiment (SANS or SAXS) to quantitatively analyse grain growth and precipitate nucleation during transient heating on a larger scale. This would allow the effects of thermal exposure to be observed in real time, potentially identifying metastable phases and tracking the formation of specific precipitate phases. It may also enable slower forming Z-phase or laves phases to be identified, although these are normally observed after long-term thermal ageing. These methods would be beneficial in locating and distinguishing smaller precipitates which cannot be analysed by SEM. Through the STEM-EDX technique the nitrogen content of the sample could also be better estimated. This may verify the lack of precipitates in the 500 transient sample if the nitrogen is causing an increase in austenite stability. Another extension would be to conduct a proton irradiation experiment prior to the laser transient testing to see whether they have the potential to repair radiation damage. It has been reported that annealing at 650°C has the capability to fully recover samples of HT9 steel up to a radiation dose of 100.3dpa [36]. It would therefore be of interest to see how the impacts of radiation

damage and thermal transients combine and whether transients at similar temperatures of 700°C would create the same effect. This would be of great advantage to the structure of the first wall. Separate to Eurofer 97, other fusion structural materials should similarly be tested to investigate the effects of thermal transients on their microstructures. ODS Eurofer 97, RAFM castable nanoalloys, and P91 steel are among those for which laser exposure will be most relevant, however ceramic coated steels are also a potential for experimentation.

5. Conclusions

Despite their mitigation via shattered pellet injection, plasma disruptions in DEMO will pose a significant thermal degradation hazard to the structural materials of the plasma-facing first wall. For the present WCLL design, each mitigated disruption is predicted to briefly expose the Eurofer 97 underlying the FW to temperatures of up to 956°C. Eurofer 97 will remain above its 550°C design maximum temperature for approx. 2.4 seconds. Up to 2600 mitigated disruptions are expected over ITER's 30-year operating life. While the number for DEMO should be lower due to technological advances, a single thermal transient at 700°C was found sufficient to significantly alter the normalised and tempered ferritic/martensitic microstructure of as-received Eurofer 97, causing partial grain recrystallisation and coarsening of Eurofer 97's normalised and tempered ferritic/martensitic microstructure. Further transient exposure resulted in further grain coarsening, and the nucleation of many Cr-rich $M_{23}C_6$ precipitates at grain boundaries. Existing $M_{23}C_6$ and MX-type precipitates were also found to coarsen. The hardness of Eurofer 97 exposed to 850°C transients was significantly decreased, suggesting that other key mechanical properties of Eurofer 97 at the first wall may also evolve over time during service. Eurofer 97's corrosion resistance and thermal properties may also be affected. To prevent this, the frequency of mitigated disruptions during DEMO's operating lifetime must be minimised.

These results demonstrate the importance of further research on the tungsten-Eurofer 97 interface, in particular, the use of functionally graded W/Eurofer 97. Given the extreme differences in grain morphology after heating it is possible that the disruption mitigation targets for DEMO are too low to allow for long term function and efficacy of the front wall. It is currently designed to withstand a thermal load of 1 MW/m^2 [8] but, with an estimated load during disruptions of 1-2 GW/m^2 the effects will quickly start to impact the reactors performance [9].

Declarations of Competing Interest

The authors declare that they have no competing financial interests or personal relationships that have influenced the work reported in this paper.

Acknowledgements

The authors wish to thank the Karlsruhe Institute of Technology for supply of the Eurofer 97 rolled plate provided to UKAEA This work has been carried out as part of the EPSRC Centre for Doctoral Training on Nuclear Energy Futures [grant number EP/S023844/1] and within the framework of the EUROfusion Consortium, funded by the European Union via the Euratom Research and Training Programme (Grant Agreement No 101052200—EUROfusion) and from the EPSRC [grant number EP/W006839/1]. Dr Fabio Moro is thanked for providing a 3D model of the WCLL. Dr C. Jones, Dr M. Zimina, Roscoe De Cabras, Marlowe Bentham, Suki Potter-Martin, Newt Tipping and Pebbles Tipping are thanked for their support.

References

[1] K. McClements, '56th Culham Plasma Physics Summer School: Plasma Instabilities', Culham Centre for Fusion Energy, Aug. 2019.

[2] G. F. Matthews *et al.*, 'Melt damage to the JET ITER-like Wall and divertor', *Phys. Scr.*, vol. T167, p. 014070, Feb. 2016, doi: 10.1088/0031-8949/T167/1/014070.

[3] S. A. Grashin *et al.*, 'ITER-grade tungsten limiters damage under high turbulent heat flux in the T-10 tokamak', *Fusion Engineering and Design*, vol. 146, pp. 2100–2104, Sep. 2019, doi: 10.1016/j.fusengdes.2019.03.115.

[4] Z. Yang *et al.*, 'The study of heat flux for disruption on experimental advanced superconducting tokamak', *Physics of Plasmas*, vol. 23, no. 5, p. 052502, May 2016, doi: 10.1063/1.4948494.

[5] R. Wenninger *et al.*, 'The DEMO wall load challenge', *Nucl. Fusion*, vol. 57, no. 4, p. 046002, Feb. 2017, doi: 10.1088/1741-4326/aa4fb4.

[6] P. C. de Vries, M. F. Johnson, and I. S. and, 'Statistical analysis of disruptions in JET', *Nucl. Fusion*, vol. 49, no. 5, p. 055011, Apr. 2009, doi: 10.1088/0029-5515/49/5/055011.

[7] S. Ciattaglia, G. Federici, L. Barucca, A. Lampasi, S. Minucci, and I. Moscato, 'The European DEMO fusion reactor: Design status and challenges from balance of plant point of view', in *2017 IEEE International Conference on Environment and Electrical Engineering and 2017 IEEE Industrial and Commercial Power Systems Europe (EEEIC / I CPS Europe)*, Jun. 2017, pp. 1–6. doi: 10.1109/EEEIC.2017.7977853.

[8] F. Maviglia *et al.*, 'Wall protection strategies for DEMO plasma transients', *Fusion Engineering and Design*, vol. 136, pp. 410–414, Nov. 2018, doi: 10.1016/j.fusengdes.2018.02.064.

[9] F. Maviglia *et al.*, 'Integrated design strategy for EU-DEMO first wall protection from plasma transients', *Fusion Engineering and Design*, vol. 177, p. 113067, Apr. 2022, doi: 10.1016/j.fusengdes.2022.113067.

[10] T. E. Gebhart, L. R. Baylor, M. N. Ericson, S. J. Meitner, A. L. Qualls, and D. A. Rasmussen, 'Recent progress in shattered pellet injection technology in support of the ITER disruption mitigation system', *Nuclear Fusion*, vol. 61, no. 10, p. 106007, 2021.

[11] J. Wesley, 'Disruption Avoidance and Mitigation Challenges for ITER and Beyond', presented at the 5th Workshop on MHD Stability Control and Joint US-Japan Workshop, University of Wisconsin, Madison, WI, Nov. 15, 2010. Accessed: Jun. 02, 2023. [Online]. Available: https://www.google.com/search?hl=en&q=Wesley,+J.+2010.+Disruption+Avoidance+and+Mitigation+Challenges+for+ITER+and+Beyond,+15th+Workshop+on+MHD+Stability+Control+and+Joint+US-Japan+Workshop,+15-17+November+2010,+University+of+Wisconsin+Madison+WI

[12] D. Kumar *et al.*, 'The Effects of Fusion Reactor Thermal Transients on the Microstructure of Eurofer-97 Steel', *Journal of Nuclear Materials*, p. 153084, May 2021, doi: 10.1016/j.jnucmat.2021.153084.

[13] L. Stratil, H. Hadraba, J. Bursik, and I. Dlouhy, 'Comparison of microstructural properties and Charpy impact behaviour between different plates of the Eurofer97 steel and effect of isothermal ageing', *Journal of Nuclear Materials*, vol. 416, no. 3, pp. 311–317, Sep. 2011, doi: 10.1016/j.jnucmat.2011.06.018.

[14] P. Fernández, A. M. Lancha, J. Lapeña, M. Serrano, and M. Hernández-Mayoral, 'Metallurgical properties of reduced activation martensitic steel Eurofer'97 in the as-received condition and after thermal ageing', *Journal of Nuclear Materials*, vol. 307–311, pp. 495–499, Dec. 2002, doi: 10.1016/S0022-3115(02)01013-9.

[15] V. B. Oliveira, H. R. Z. Sandim, and D. Raabe, 'Abnormal grain growth in Eurofer-97 steel in the ferrite phase field', *Journal of Nuclear Materials*, vol. 485, pp. 23–38, Mar. 2017, doi: 10.1016/j.jnucmat.2016.12.019.

[16] E. Martelli, G. Caruso, F. Giannetti, and A. Del Nevo, 'Thermo-hydraulic analysis of EU DEMO WCLL breeding blanket', *Fusion Engineering and Design*, vol. 130, pp. 48–55, May 2018, doi: 10.1016/j.fusengdes.2018.03.030.

[17] F. Edemetti, E. Martelli, A. Tassone, G. Caruso, and A. D. Nevo, 'DEMO WCLL breeding zone cooling system design: Analysis and discussion', *Fusion Engineering and Design*, vol. 146, pp. 2632–2638, Sep. 2019, doi: 10.1016/j.fusengdes.2019.04.063.
[18] K. Mergia and N. Boukos, 'Structural, thermal, electrical and magnetic properties of Eurofer 97 steel', *Journal of Nuclear Materials*, vol. 373, no. 1, pp. 1–8, Feb. 2008, doi: 10.1016/j.jnucmat.2007.03.267.
[19] M. Rieth, 'Material Property Handbook on Eurofer 97', Eurofusion Power Plant Physics and Technology Dept., MAT-1.2.1-T006-D002, 2016.
[20] J. Gaspar *et al.*, 'Emissivity measurement of tungsten plasma facing components of the WEST tokamak', *Fusion Engineering and Design*, vol. 149, p. 111328, Dec. 2019, doi: 10.1016/j.fusengdes.2019.111328.
[21] I. A. Maione, M. Roccella, A. Marin, C. Bertolini, and F. Lucca, 'A complete EM analysis of DEMO WCLL Breeding Blanket segments during VDE-up', *Fusion Engineering and Design*, vol. 146, pp. 198–202, Sep. 2019, doi: 10.1016/j.fusengdes.2018.12.017.
[22] S. Nunez-Sanchez, H. D. Andrade, J. Harwood, I. Bickerton, N. A. Fox, and M. J. Cryan, 'Molybdenum gratings as a high-temperature refractory platform for plasmonic heat generators in the infrared', *Micro and Nano Letters*, vol. 13, no. 9, pp. 1325–1328, 2018, doi: 10.1049/mnl.2018.0156.
[23] H. Dominguez-Andrade, A. Croot, G. Wan, J. A. Smith, and N. A. Fox, 'Characterisation of thermionic emission current with a laser-heated system', *Review of Scientific Instruments*, vol. 90, no. 4, p. 045110, Apr. 2019, doi: 10.1063/1.5088150.
[24] Synrad Inc., 'v40 Firestar Operators Manual'. Accessed: Oct. 07, 2020. [Online]. Available: https://synrad.com/sites/default/files/2017-06/Operators%20Manual%20v40.pdf
[25] A. D. Warren, A. I. Martinez-Ubeda, O. D. Payton, L. Picco, and T. B. Scott, 'Preparation of Stainless Steel Surfaces for Scanning Probe Microscopy', *Microscopy Today*, vol. 24, no. 3, pp. 52–55, May 2016, doi: 10.1017/S1551929516000341.
[26] D. Tomus and H. P. Ng, 'In situ lift-out dedicated techniques using FIB–SEM system for TEM specimen preparation', *Micron*, vol. 44, pp. 115–119, Jan. 2013, doi: 10.1016/j.micron.2012.05.006.
[27] K. Jiang, E. Martelli, P. Agostini, S. Liu, and A. Del Nevo, 'Investigation on cooling performance of WCLL breeding blanket first wall for EU DEMO', *Fusion Engineering and Design*, vol. 146, pp. 2748–2756, Sep. 2019, doi: 10.1016/j.fusengdes.2019.05.018.
[28] M. Klimenkov, R. Lindau, E. Materna-Morris, and A. Möslang, 'TEM characterization of precipitates in EUROFER 97', *Progress in Nuclear Energy*, vol. 57, pp. 8–13, May 2012, doi: 10.1016/j.pnucene.2011.10.006.
[29] B. Yan *et al.*, 'The Effect of Precipitate Evolution on Austenite Grain Growth in RAFM Steel', *Materials*, vol. 10, no. 9, Art. no. 9, Sep. 2017, doi: 10.3390/ma10091017.
[30] T. Loewenhoff *et al.*, 'Impact of combined transient plasma/heat loads on tungsten performance below and above recrystallization temperature', *Nucl. Fusion*, vol. 55, no. 12, p. 123004, Oct. 2015, doi: 10.1088/0029-5515/55/12/123004.
[31] H. K. Danielsen, 'Review of Z phase precipitation in 9–12 wt-%Cr steels', *Materials Science and Technology*, vol. 32, no. 2, pp. 126–137, Jan. 2016, doi: 10.1179/1743284715Y.0000000066.
[32] A. Danón and A. Alamo, 'Behavior of Eurofer97 reduced activation martensitic steel upon heating and continuous cooling', *Journal of Nuclear Materials*, vol. 307–311, pp. 479–483, Dec. 2002, doi: 10.1016/S0022-3115(02)01209-6.
[33] P. Fernandez, A. M. Lancha, J. Lapena, M. Serrano, and M. Hernandez-Mayoral, 'Reduced Antivation Ferritic/Martensitic Steel Eurofer 97 as Possible Structural Material for Fusion Devices. Metallurgical Characterization on As-Received Condition and after Simulated Services Conditions', Jul. 2004, Accessed: Jun. 02, 2023. [Online]. Available: https://www.osti.gov/etdeweb/biblio/20572316
[34] B. Shang *et al.*, 'Effects of grain boundary characteristics changing with cold rolling deformation on intergranular corrosion resistance of 443 ultra-pure ferritic stainless steel', *Corrosion Communications*, vol. 8, pp. 27–39, Dec. 2022, doi: 10.1016/j.corcom.2022.07.002.

[35] F. Stein and A. Leineweber, ‘Laves phases: a review of their functional and structural applications and an improved fundamental understanding of stability and properties’, *J Mater Sci*, vol. 56, no. 9, pp. 5321–5427, Mar. 2021, doi: 10.1007/s10853-020-05509-2.
[36] T. S. Byun, J.-H. Baek, O. Anderoglu, S. A. Maloy, and M. B. Toloczko, ‘Thermal annealing recovery of fracture toughness in HT9 steel after irradiation to high doses’, *Journal of Nuclear Materials*, vol. 449, no. 1, pp. 263–272, Jun. 2014, doi: 10.1016/j.jnucmat.2013.07.064.